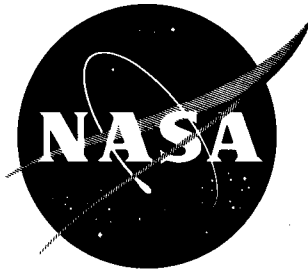


32p.



N 63 18653

CODE-1

# TECHNICAL NOTE

D-1411

ADDITIONAL STUDIES OF SCREEN AND ACCELERATOR GRIDS  
FOR ELECTRON-BOMBARDMENT ION THRUSTORS

By William R. Kerslake and Eugene V. Pawlik

Lewis Research Center  
Cleveland, Ohio

NATIONAL AERONAUTICS AND SPACE ADMINISTRATION  
WASHINGTON

August 1963

NATIONAL AERONAUTICS AND SPACE ADMINISTRATION

---

TECHNICAL NOTE D-1411

---

ADDITIONAL STUDIES OF SCREEN AND ACCELERATOR GRIDS  
FOR ELECTRON-BOMBARDMENT ION THRUSTORS

By William R. Kerslake and Eugene V. Pawlik

SUMMARY

18653

An investigation of accelerator-grid systems was made with three ion thrusters having 5-, 10-, and 20-centimeter-diameter electron-bombardment ion sources. Mercury ion beams of 0.01 to 0.7 ampere were generated at net accelerating voltages of 600 to 7000 volts. Grid geometry was studied to determine the effect of hole shape, spacing, and grid thickness upon the ion focusing of the accelerator system and the fraction of Child's law current passed. Geometric limits for acceptable thruster performance values are discussed. Grid temperature profiles were obtained to evaluate accelerator warping problems. Graphite grids were tested and found to be a solution to these problems for laboratory testing. The method of calculating thrust from metered electrical parameters was verified with a pendulum-type thrust target.

INTRODUCTION

The electron-bombardment ion thruster described in references 1 and 2 is a mechanically simple and reliable device. Further work on this thruster has been reported in references 3 to 8. In the study described herein, the accelerator tests on a 10-centimeter-diameter thruster presented in reference 5 have been extended. In the preceding investigation, a multihole plate accelerator grid was found to have good accelerator performance. That is, it had a current capacity near the Child's law limit, and it had low impingement. This grid also offered structural advantages and gains in accelerator perveance when compared with a wire grid. Limits of grid spacing and electrical breakdown were defined, and suitable grid materials were determined.

In this report the accelerator hole shape, size, and spacing were investigated further. A limit on the screen thickness was established. Effects of similar accelerator-grid configurations with different thruster sizes were also determined. The study was extended to 5-, 10-, and 20-centimeter-diameter thrusters whose grid spacing was varied from 0.079 to 0.544 centimeter. The thrusters were operated at beam currents ranging from 0.011 to 0.700 ampere with most of the data recorded at 0.125 ampere. The range of net accelerating voltages investigated was 600 to 7000 volts, which corresponds to a range in specific impulse of 2400 to 8400 seconds.

The effects of thermal expansion and the resulting grid warpage were determined, and temperature profiles were obtained as a function of time for both the screen and the accelerator. Graphite grids were studied as a possible solution to thermal expansion problems.

A pendulum-type, cone-shaped thrust target was placed in the ion beam and verified the values of thrust calculated from the electrically metered thruster output.

## APPARATUS

The three sizes of ion thrusters used in this experiment produced 5-, 10-, and 20-centimeter-diameter exhaust beams. A typical electron-bombardment ion thruster is shown in a cutaway sketch in figure 1. The 10-centimeter source was identical to the one used in the previous accelerator investigation (ref. 5). The 5- and 20-centimeter sources were scaled from the 10-centimeter source and were geometrically similar (ref. 3).

During thruster operation, mercury was vaporized in a steam-heated boiler held approximately at a constant temperature. The propellant flow was controlled by interchangeable sharp-edged orifices. The orifices used were the same calibrated orifices described in reference 5.

Propellant vapor from the boiler flowed into the ionization chamber through a flow distributor. The ion chamber contained a cylindrical anode with a length-to-diameter ratio of about 1. A thermionic electron emitter, a hairpin-shaped tungsten wire, was located on the axis of the chamber. An axial magnetic field increased the probability of collision between the emitted electrons and the mercury propellant by preventing the rapid escape of the electrons to the anode. The electromagnet used was arranged as recommended in reference 4 to provide a tapered field with a downstream- to upstream-strength ratio of approximately 0.6 through the ion chamber. The downstream field was measured at the screen grid and the upstream field at the center of the distributor.

During thruster operation, the electron bombardment of the mercury propellant produced a plasma within the ion chamber. The electrons in this plasma were extracted at the anode, while the majority of the ions that diffused to the screen at the downstream end of the chamber were accelerated to form the ion beam.

The accelerating system was composed of a pair of grids, which are designated the screen and the accelerator. These two grids were aligned and electrically insulated by aluminum oxide spheres as shown in figure 1. The spacing between the grids was determined by the size of the sphere used.

Figure 2 and table I present details of 12 grid sets that were tested. Grid alignment was obtained by match drilling the holes. The grids were fabricated from initially flat plates and were straightened and stress relieved to eliminate any warpage that occurred during machining. Some warping due to temperature gradients usually occurred during thruster operation.

The ion thrusters used in this experiment were mounted either in a bell jar connected to a large vacuum tank or, as in the case of the 20-centimeter thruster, within the vacuum tank itself. Only one thruster was operated at a time. The bell jar was the preferable location for ease of operational changes. The tank location was used when a larger operating space was needed as with the 20-centimeter-diameter thruster and the thrust target installation. The bell jar was 20 inches in diameter and was connected by a 12-inch gate valve to a 5-foot-diameter by 16-foot-long vacuum tank. The tank was evacuated by three 32-inch-diameter oil diffusion pumps. The vacuum facility is described more fully in reference 9. Figure 3 shows a cutaway view of the facility with a thruster mounted in each of the two testing positions. The liquid-nitrogen-cooled condenser and thrust target are also shown in this figure. The ion beam in all cases was neutralized by an electron-emitter wire strung across the exhaust beam about 25 centimeters downstream of the thruster.

The liquid-nitrogen-cooled surfaces had an area of approximately 33 square meters, which, together with the diffusion pumps, enabled the tank to be evacuated to  $2 \times 10^{-6}$  torr and the bell jar to  $1 \times 10^{-5}$  torr when the thrusters were not operating. With ion thruster operation in the bell jar, pressure rose to approximately  $2 \times 10^{-5}$  torr. The tank pressure rose to about  $5 \times 10^{-6}$  torr for either location of thruster operation.

A pendulum-type thrust target was mounted in the ion exhaust beam. Details of the target and its mounting are shown in figure 4. A cone shape was chosen for the target so that most of the sputtered and rebounding particles would be contained by the target, which would reduce any error caused by the momentum of the sputtered particles. This shape was also chosen to provide sufficient area for radiation cooling. The cone was constructed of 0.03-millimeter-thick stainless steel. The cone diameter was 25 centimeters, and the length was 50 centimeters. The cone entrance was located about 40 centimeters downstream of the accelerator grid. The target mass was 60 grams and was supported by four 0.013-centimeter-diameter tantalum wires. An aluminum fin on the bottom of the target was passed through the gap of a C-shaped permanent magnet to dampen oscillations. Thrust target deflections were determined optically with a cathetometer.

## PROCEDURE

Prior to and after each accelerator test, the assembled grid spacing was measured in five locations. The average grid separation values are presented in table II. The thruster was mounted in the vacuum facility and pumped down to the desired vacuum conditions. Steam was supplied to the boiler to start the propellant flow, and, after a short period of time (3 to 5 min), the system reached operating temperature. Voltages were then applied to the thruster. A schematic drawing of the power supplies and the thruster connections is shown in figure 5. To initiate the discharge, it was usually necessary to raise the discharge chamber voltage to about 70 volts, but, during thruster operation, the discharge chamber voltage was set at 50 volts. It has been found (ref. 10) that at this voltage difference doubly charged ions constitute 5 percent or less of the ion beam. The anode potential was maintained at the desired positive or net accelerating voltage. The screen, the distributor, and the filament were physically

connected to the thruster body and consequently were at the same potential. A negative voltage was applied to the accelerator to prevent electron backstreaming from the tank to the thruster. Backstreaming, in addition to causing undesirable arcing from the tank environment to the thruster, could cause the ground current meter (beam current) to read high by several percent to several hundred percent.

For each grid configuration, acceleration voltages were varied from a minimum value where accelerator impingement increased sharply to a maximum where breakdown voltages were obtained. Data were taken for constant values of beam current  $J_B$  and  $R$  (where  $R$  is defined as  $V_I/(V_I + |V_A|)$ , the ratio of net to total acceleration voltage). (All symbols are defined in the appendix.) Each of the three sizes of thrusters was operated with its ion source held approximately constant. Small changes were made in filament heating current (filament emission) to maintain the thruster at a constant beam current. The discharge chamber voltage  $\Delta V_I$  was held constant at 50 volts for all three sizes. The magnetic field strength, while approximately constant for each size thruster, was varied between sizes as listed in table III.

The thruster was usually operated near a constant propellant utilization  $\eta_u$  of 0.8 (ion beam current out divided by equivalent current of neutral mercury flow in). Runs 6(a) and 8 (table II) were run at a lower propellant utilization because of operational limits with these designs. Since the mercury flow from the boiler for these runs corresponded to 0.161 ampere, the utilization can be obtained by dividing the beam current by this value.

## RESULTS AND DISCUSSION

The 12 sets of grids were tested over ranges of accel-decel voltages. A summary of accelerator data and results is presented in table II. A more detailed compilation of data is presented in table III. The actual value of accelerator current  $J_A$  measured was the sum of ion impingement plus secondary electron emission. The amount of secondary electrons produced by  $Hg^{+1}$  ions on molybdenum at several thousand electron volts, however, is thought (by a comparison with cesium ion bombardment on molybdenum surfaces, ref. 11) to be less than 10 percent and probably only about 2 percent of impingement current. Therefore, the secondary electron effect has been neglected.

Impingement current  $J_A$  is plotted against net acceleration voltage  $V_I$  for several values of  $R$  in figure 6 for two typical screen-accelerator sets. Impingement curves for the other grid sets are similar to figure 6(a) and were not plotted but are available from the data in table III.

For each grid set, a region of acceleration voltages was observed where fairly low values of impingement existed. As the net acceleration voltage was lowered, a condition was reached where the ions were supplied at a rate that approached the space-charge-limited flow, which caused the accelerator impingement current to rise. The total acceleration voltage just before this rise was used to calculate the theoretical space-charge-limited beam current for comparison with experimental beam current values. The anode voltage was divided by  $R$  to obtain  $\Delta V$  for use in the following form of Child's law equation:

$$J_S = \frac{8}{9} \epsilon_0 \sqrt{\frac{q}{2m}} \frac{A_0 (\Delta V)^{3/2}}{l^2} = 0.386 \times 10^{-8} \frac{A_0 (\Delta V)^{3/2}}{l^2} \quad (1)$$

where

- $J_S$  space-charge-limited beam current, amp  
 $\epsilon_0$  permittivity of free space,  $8.85 \times 10^{-12}$  coulomb<sup>2</sup>/((newton)(m))<sup>2</sup>  
 $q/m$  charge-to-mass ratio,  $0.4811 \times 10^6$  coulomb/kg for Hg<sup>+1</sup>  
 $A_0$  screen grid open area, sq cm  
 $\Delta V$  total acceleration voltage,  $V_I + |V_A|$ , v  
 $l$  acceleration distance between grids, cm

Table II lists screen-accelerator grid spacings, the potential at the knee of each impingement curve, the electrical breakdown voltage, the percent of beam impingement at the knee of the impingement curve, and the experimental beam current (expressed as a fraction of the calculated ideal Child's law current). Since the grid thickness was not negligible as compared to the grid spacing, the ratio of beam current to theoretical Child's law current was calculated on the basis of both the centerline and surface gap grid spacing.

Ion chamber losses as described by the discharge energy dissipated per beam ion were calculated for each operating point and are presented in table III. These ion chamber losses can be represented as the ion discharge chamber voltage  $\Delta V_I$  multiplied by the difference between the anode and the beam currents and divided by the beam current.

### Accelerator Hole Effects

Three different grid systems were studied to determine the effect of hole geometry on accelerator performance:

- (1) Beveled hole shape in the screen grid, grid sets 1 to 4
- (2) Accelerator holes smaller than screen holes, grid set 5
- (3) A set of small-hole grids, grid set 6

It was believed that a beveled hole could approximate the ideal beam-focusing methods of Pierce (ref. 12). The screen was beveled at angles of 33° (grid set 1) and 45° (grid set 2) as shown in figure 2. These beveled grids were first tested and reported in reference 5. Grid sets 1 and 2 were also reversed (grid sets 3 and 4, respectively) to examine the effects of the beveled geometry on the beam extraction.

Although reference 5 indicated that with the bevel on the screen hole the impingement current was lower than normal, it is believed that the data in this

report are more correct. The data of reference 5 were recorded under conditions of irreproducibly low bell jar pressures. The data in this report (about three times more data) indicate a mean impingement value of about 1 percent for either screen bevel angle. This value is consistent with the impingement currents of other grid sets in both this report and reference 5 and indicates that there is no significant increase in beam focusing with either type of beveled hole configuration.

Figure 7 presents a comparison of the performance of the beveled screens in the forward and reversed positions. Over the range of  $l/D$  from 0.7 to 1.1, the reversed screens passed a higher fraction of Child's law current than the forward screens. There was no consistent trend of fraction of Child's law current with  $l/D$  between the  $33^\circ$  and  $45^\circ$  grids. It is also indicated in table III that impingement currents were equivalent for reversed and forward operation. When  $l/D$  of grid set 2 ( $45^\circ$ ) was increased to 1.38, the thruster, because of electrical breakdown, would only operate at reduced beam currents. No further attempts were made to increase  $l/D$  beyond 1.1.

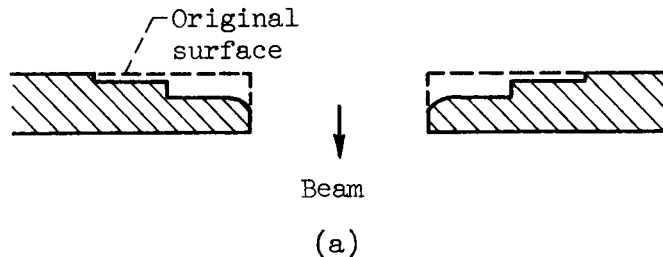
Grid set 5 (fig. 2(b)) was designed with normal (0.476 cm) screen holes but with each corresponding accelerator hole reduced to one-ninth the area of the screen hole. A design such as set 5 might improve the accelerator grid lifetime by providing more web material between holes. It has been shown in reference 8 that after a 150-hour endurance run the major accelerator grid erosion was to the sides of the hole, while the grid plate thickness remained relatively unchanged. Thus, by enlarging the web thickness, more material was added to the region of greatest wear. The present investigation was limited to studying the problems of focusing the ion beam into the smaller accelerator hole. No attempt was made to determine the ultimate lifetime.

As seen in table III for run 5, the ion source was operated to maintain a constant beam current of 0.075 ampere with variations in acceleration voltage. The fraction of beam current passing through the accelerator (defined as  $J_B/(J_B + J_A)$ ) varied from 0.55 to 0.97. Typical operation is shown for run 5(a) in table III where, for  $\Delta V > 3800$  volts, 0.9 of the beam was focused into the accelerator hole. At lower total acceleration voltages, beam spreading caused by the increased charge density of the slower ions rapidly increased the accelerator impingement. At higher total acceleration voltages the fringes of the beam were better focused into the hole, and 0.97 of the beam ions could be passed through.

Run 5 was made at a reduced magnetic field of 11 to 16 gauss because, in so doing, the accelerator impingement current (for reasons not presently understood) was greatly reduced. For example, at a normal magnetic field of 35 gauss, the impingement increased to  $25 \times 10^{-3}$  ampere from a value of  $5 \times 10^{-3}$  ampere at 11 gauss; however, at the lower magnetic field conditions, the ion chamber discharge energy (ev per ion) was approximately double that at normal magnetic field conditions.

Figure 8 consists of photographs of the upstream face of the accelerator grid with one random hole near the center of the grid marked for reference. After thruster operation of approximately 2.3 hours at an average impingement current of 0.006 ampere, the photograph in figure 8(b) was made. It shows a

lightly sputtered region that is approximately the same size as that of the screen hole. The photograph shown in figure 8(c) was taken after run 5(c) was made at a high impingement current of 0.060 ampere for 0.75 hour. The upstream face of the accelerator grid has been eroded away as shown in sketch (a), which is drawn from figure 8(c).



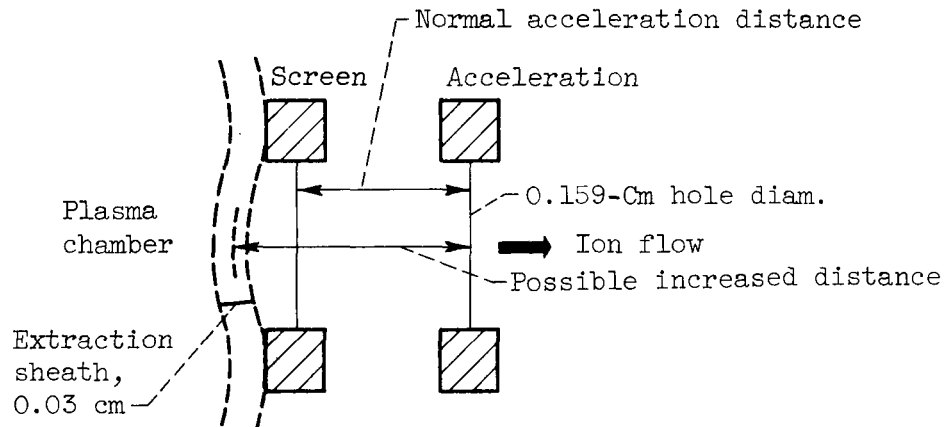
The erosion pattern of the type shown in the sketch is caused by direct ion beam impingement. If the accelerator grids had been operated only at high accelerating voltages where direct impingement was minimized, the erosion of the upstream face would not have been so severe.

It appears that, since 0.97 fraction of the beam was passed at the point of lowest impingement in run 5(a), the use of a thicker web between accelerator grid holes should lead to a longer accelerator lifetime, but it may be that a smaller maximum current density can be passed. Also, as the beam must pass through a smaller accelerator hole, physical tolerances become increasingly important. A sufficient accuracy of hole location for a 0.476-centimeter accelerator hole may be  $\pm 0.007$  centimeter, but, for a 0.159-centimeter hole location, the tolerance may be  $\pm 0.002$  centimeter.

Another geometric variable tested was the diameter to which both the screen and accelerator holes could be reduced. This variable was selected because past data indicated that, because of a grid aperture effect (distortion of electric field lines in the vicinity of a hole), the beam perveance could be increased as the hole diameters were reduced, and thus a constant accelerating distance is kept. The reduced hole size (0.159-cm diam.) of grid set 6 was selected as the smallest size consistent with the thickness of the plates used and the tolerance of fabrication and assembly. The screen and accelerator thicknesses of 0.051 and 0.102 centimeter, respectively, were believed to be the minimum necessary for rigid construction of a 10-centimeter-diameter thruster. The anticipated trend of higher beam perveance for grid set 6 was not fully realized, and the actual fraction of Child's law current fell lower than that of the larger 0.476-centimeter-diameter hole size (grid set 10) or the 0.315- and 0.238-centimeter hole size data of reference 5.

The performance noted with smaller hole accelerator grids may indicate an unfavorable interaction occurring between the ion chamber plasma and the extraction holes of the screen grid. Calculated Debye length for ion chamber plasma conditions is only about 0.005 centimeter, but the calculated extraction sheath thickness between the discharge and screen is about 0.03 centimeter (see sketch (b)).





(b)

The 0.03-centimeter sheath thickness is about one-fifth of the 0.159-centimeter screen hole diameter. As the hole diameter becomes smaller (compared to the width of the extraction sheath), the effective total acceleration distance may increase from the center-of-screen thickness to a point closer to the extraction sheath. This increase in the effective total acceleration distance would have the result of reducing the fraction of Child's law current passed, as based on the usual center of thickness spacing. The anticipated fraction of Child's law current without this increased distance was about 0.8 (as determined both by experimental data of other, larger-hole grids at a similar  $l/D$  and by a "grid aperture effect" calculation using the methods of appendix B in ref. 5), while the measured value was about 0.6. An increased effective acceleration distance would also mean a longer ion acceleration time during which random motion would be greater and presumably accelerator impingement could increase. The measured impingement was high and always remained above 1 percent of the beam.

Slotted plates (grid set 7) were constructed as an intermediate design between the wire grid accelerators of reference 2 and the multihole accelerator. This approach was considered since the ion chamber performance for the wire grids was better than that of the drilled plates which, however, were able to pass a greater fraction of Child's law current. Alinement of this new grid set was maintained by simultaneous milling of the slots in both plates. The slotted plates had an open area of 56 square centimeters, which is the largest of any 10-centimeter set tested. As expected, the discharge chamber energy for the slotted accelerators was low. The thermal warpage for this grid configuration was comparable with that for the drilled plates, whereas the wire grids (as reported in ref. 2) expanded and bowed considerably during a typical run. The fraction of Child's law current was found to be lower for the slotted accelerators, but was essentially compensated for by the increased open area.

It was also found necessary to operate with a lower value of  $R$  to stop electron backstreaming. The probable explanation for this is that for a given slot width or hole diameter the holes maintain a more uniform electric field across the grid opening. A slot opening (with a many times longer length than width) permits more field distortion to occur, and, thereby, electrons may find

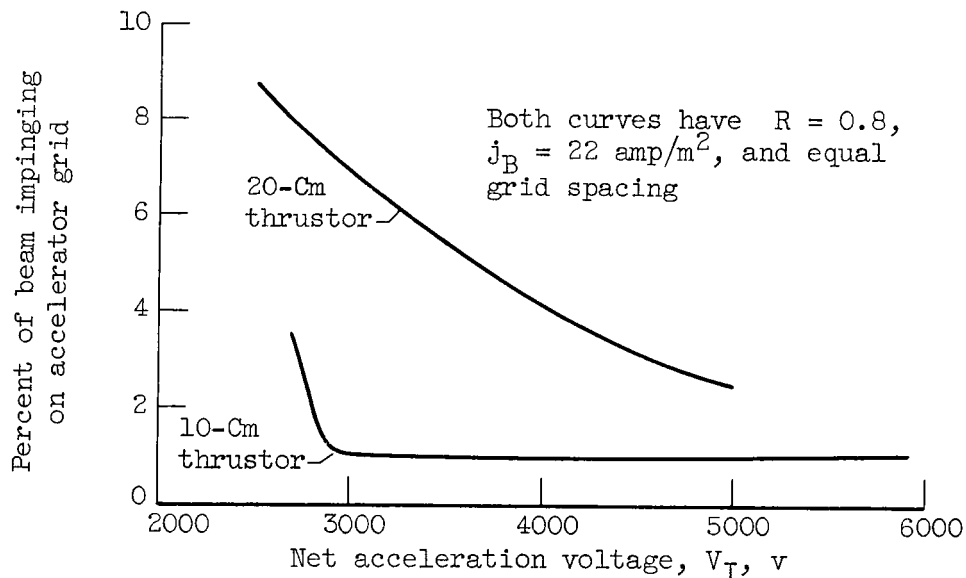
a backstreaming path through the accelerator field at a lower value of  $R$ .

### Thick Screen

A thick screen (grid set 8) was used to raise the ion chamber pressure by reducing the flow conductance through the grids. It was assumed that a higher ion chamber pressure would result in a longer neutral residence time and a corresponding increase in propellant utilization efficiency. The resulting thruster operation was very erratic with extremely high values of discharge chamber energy ranging from 3800 to 9320 electron volts per ion. Although the neutral flow was sufficient to supply a 0.125-ampere beam at 0.80 propellant utilization efficiency, the actual value remained low (0.040 to 0.050 amp). The thick screen shields the plasma from the field of the accelerator and thereby impedes ion extraction.

### Thruster Size Effects

Geometrically similar 5- and 20-centimeter sources were scaled from the 10-centimeter source. Identically drilled grids were constructed (grid sets 10, 11, and 12) and run with the three thruster sizes. Data were obtained at approximately the same grid spacing. If a magnetic field was used that was consistent with minimum discharge energy for each size thruster (see table III or fig. 6, ref. 4), the discharge energy per beam ion was found to be essentially constant for a given specific impulse over the size range of thrusters considered. The accelerator performance was similar for the two smaller thrusters and somewhat reduced for the 20-centimeter size, as evidenced by higher impingement current and a lower fraction of Child's law current. The impingement curve knee values for the 20-centimeter thruster were not very well defined, as can be seen from figure 6(b). Sketch (c) is included to compare directly the shapes of the impingement curves for the 10- and 20-centimeter-diameter thrusters.



(c)

Beam current density profiles were obtained during the 20-centimeter thruster operations in the manner described in reference 5. A high beam current density region was measured near the axis. The broader knee for the 20-centimeter thruster is attributed to this concentration of ions near the center of the accelerator system and the consequent approach to space-charge-limited flow at higher voltage. The outer edges of the 20-centimeter thruster tend to receive few ions because of the concentrated discharge at the ion chamber axis. With the 10-centimeter thruster a high-density region also existed at the axis; but, because a lower total beam current was required, its peak ion density was proportionally lower, and the width of the peak was a greater fraction of the thruster diameter. The lower voltage knee of the 10-centimeter thruster can be attributed to ion acceleration through a greater fraction of the accelerator total area. The sharper knee may indicate that a larger percentage of the total flow area is approaching space-charge-limited flow at the same acceleration voltage.

### Temperature Profile

One of the problems associated with the accelerator grids tested in this report was warping due to thermal expansion. To investigate the temperature profiles of the grids, thermocouples were mounted on the screen and accelerator grids. For a 0.125-ampere ion beam under typical operating conditions, the center of both screen and accelerator reached steady-state temperatures of approximately 800° to 900° F. The edges of both grids were cooler (by 100° to 250° F) than the centers with the steeper temperature gradient existing in the accelerator rather than in the screen. The accelerator warping due to a steeper temperature gradient was usually more severe than that of the screen. The temperature of the grids rose rapidly in the first 10 to 15 minutes of operation and then gradually leveled off to a steady-state value. Typical heat-up curves for two locations on the screen for beam currents of 0.125 and 0.250 ampere are presented in figure 9. One thermocouple was located at the center of the grid and the other 4 centimeters away. A more severe temperature gradient was found to exist with higher values of beam current.

Heating of the screen appears to be due to radiation from the filament and heat contributed by the ion chamber plasma. (The former source of heating was verified by turning the mercury flow off and leaving the filament on. The temperature of the screen fell at a moderate rate but not nearly as fast as when the filament was also off.) For the accelerator, one of the primary sources of heating appears to be ion impingement. Figure 10 shows the temperature at three locations on the accelerator grid for a range of impingement currents. By operating near space-charge-limited conditions, it was possible to obtain various impingement levels by changing  $V_I$  slightly while maintaining a constant beam current of 0.125 ampere. As the impingement current was increased from 0.001 to 0.021 ampere, the temperature gradient became more severe. To verify that impingement current was responsible for the temperature rise, the following calculation was made. The accelerator grid was assumed to have a uniform initial temperature of 550° F with the thruster operating and with a negligible (0.001 amp) impingement current. Seventy watts of additional power was now uniformly applied to the grid. The 70-watt increase corresponds to an impingement current increase of 0.020 ampere at a total acceleration voltage of 3500 volts. A calculated

equilibrium temperature of 1060° F resulted from a radiation heat balance. (All accelerator-grid heat losses were assumed to have occurred by radiation of the downstream side of the grid to the cold baffles in the tank, which were assumed to be at 0° R for purposes of the calculation. An emissivity of 0.4 was used for the molybdenum grid.) The calculated equilibrium temperature compares favorably with the measured maximum 1080° F of figure 10.

Warpage considerations and fabrication techniques have been found to limit the minimum spacing between grids to aspect ratios (ratio of engine diameter to grid separation) of about 100 to 150. Variations from the average separation as great as 0.025 centimeter could be found for a typical, tested molybdenum grid set. Grid thinness is also limited by warpage considerations to values of 0.050 and 0.100 centimeter for the screen and accelerator grids, respectively. Grid materials that have already demonstrated resistance to warping and sputtering include molybdenum, stainless steel, tungsten, and tantalum (ref. 5).

Accelerator plates of graphite (National Carbon Co., ATJ grade) were constructed (grid set 9) in an attempt to reduce grid warpage. This grade was selected because of its properties of low uniform thermal expansion, high density, high strength, and small grain size. The plates were drilled from a 0.155-centimeter-thick graphite sheet, which was believed to be the thinnest that would be structurally acceptable. In addition to the normal evaluation tests, the grids were run at high accelerator impingement currents that ranged from 0.040 to 0.100 ampere for a period of 15 minutes. Graphite grids showed no tendency whatever to warp at these high impingement currents, although the best metal grids would have been hopelessly warped. The grid spacing, which was measured before and after several runs, remained constant despite the severe impingement.

Run 9 yielded the expected results that a change in material did not alter the ion chamber performance. As shown in table II, the graphite grids gave performance results comparable with those of a geometrically similar molybdenum grid set (grid set 10).

The grids were disassembled and weighed before and after each run. The accelerator weight loss due to sputtering was found to be only 2.52 grams per ampere-hour of impingement current at an average total accelerating voltage of about 4000 volts. The material lost on a volume rate basis, however, was similar to that encountered with molybdenum grids.

A disadvantage of the graphite grids was the additional care required in handling and fabrication because of the brittleness of the material. The most probable use of graphite grids will be in laboratory apparatus when close tolerance and the ability to withstand short periods of high impingement are required. For space operation graphite grids do not appear to offer sufficient gains in sputtering resistance to justify the care required to protect them against breakage under high gravity loads and vibration.

#### Thrust Target

The thrust is most easily calculated from the measured ground return current

and the net acceleration potential. Large angles of beam divergence caused by accelerator system optics would, however, result in a reduction in thrust that would not be corrected in calculations based only on accelerating voltages and beam currents. These calculated thrust values were therefore checked, for several multihole grids, by the use of a target in the exhaust beam. A cone-shaped thrust target was constructed and installed as described in the section APPARATUS.

The beam thrust was determined by using the following simple pendulum formula for small angles of deflection:

$$T = W \frac{\delta}{L} \quad (2)$$

where

T beam thrust, newtons

W thrust target weight, newtons

$\delta$  thrust target deflection, m

L pendulum length, m

The length of the pendulum was determined by measuring the period of oscillation and using the following equation:

$$L = \frac{\tau^2 g}{4\pi^2} \quad (3)$$

where

$\tau$  period of oscillation, sec

g gravity constant, 9.81 m/sec<sup>2</sup>

For the thrust target used in this report, the measured period of oscillation was 1.20 seconds, which corresponded to a calculated length of 0.357 meter. The beam thrust as calculated from electrical meter readings of beam current and voltage is

$$T = \sqrt{2 \frac{m}{e} V_I} J_B \quad (4)$$

Combining equations (2) and (4) and solving for  $\delta$  yield

$$\begin{aligned} \delta &= \frac{L}{W} \sqrt{2 \frac{m}{e} J_B} \sqrt{V_I} \\ &= 1.22 \times 10^{-3} J_B \sqrt{V_I} \quad \text{for } \text{Hg}^{+1} \text{ ions} \end{aligned} \quad (5)$$

Equation (5) was used to calculate a theoretical deflection curve for various values of beam current and acceleration voltage, and this curve is shown in figure 11. The experimental, optically measured deflection data are also shown in this figure. Calculated and measured values agree to within about 10 percent at the higher thrust levels tested (above  $1.3 \times 10^{-3}$  newton). At lower thrust levels the thrust target sensitivity is less and may account for the greater percentage error. The thrust target may read 3 to 6 percent low because of 10- to 20-percent double ionization (ref. 10) for which no correction was made. It appears that there is no substantial (>10 percent) error in directed thrust because of beam spreading.

### CONCLUDING REMARKS

Certain basic design features have been established for the construction of accelerator grids for an electron bombardment thruster. They are as follows: The physical thicknesses of the grids have been established by mechanical strength requirements to resist thermal warpage. The relation of grid hole diameter to grid thickness should be 3 to 1 or greater to prevent the screen thickness from shielding the plasma from the accelerator grid and making ion extraction difficult. To minimize electric field distortion between the grid holes, a ratio of grid plate separation to hole diameter ( $l/D$ ) should be at least 0.6 to 1.0. Minimum grid plate separation has been limited by fabrication difficulties and thermal warpage to ratios of thruster diameter to grid plate separation of about 100 to 150. The maximum accelerator grid spacing is determined by space-charge flow limitations consistent with electrical breakdown and the specific impulse required.

For a 10-centimeter-diameter thruster the grids should be at least 0.1 centimeter thick with holes greater than 0.3 centimeter in diameter. The grid separation should be 0.2 to 0.3 centimeter to provide an  $l/D$  that avoids distortion and also permits an easily fabricated and warpage-resistant grid set. Material of the grids may be molybdenum, tantalum, tungsten, or stainless steel. Graphite grids offered excellent resistance to warpage but, because of brittleness, may be restricted to laboratory use.

The accelerator performance as measured by current density and impingement was found to be approximately constant as the grid diameter was reduced from the 10-centimeter thruster to a 5-centimeter size and adversely affected when increased to a 20-centimeter size. Efficient operation of a thruster larger than 20 centimeters will require a more uniform ion chamber discharge, perhaps by the use of multiple filaments. Mechanical requirements indicate that accelerator systems larger than 20 centimeters may take the form of parallel grid wires under tension, or, if a multihole grid is to be used, internal points of support may be necessary.

Thrust target measurements indicate that the thrust calculated from electrical meter readings of beam current and voltage is within 10 percent of the measured target value at thrust levels above  $1.3 \times 10^{-3}$  newton.

Lewis Research Center

National Aeronautics and Space Administration  
Cleveland, Ohio, April 12, 1963

# APPENDIX - SYMBOLS

$A_O$	grid open area, sq cm
$D$	diameter of grid hole, cm
$g$	gravity constant, $9.81 \text{ m/sec}^2$
$J_A$	accelerator current, amp
$J_B$	ion beam current, amp
$J_E$	emission current, amp
$J_I$	anode current, amp
$J_S$	space-charge-limited beam current, amp
$j_B$	ion beam current density, $\text{amp/m}^2$
$L$	pendulum length, m
$l$	acceleration distance between grids, cm
$q/m$	charge-to-mass ratio, $0.4811 \times 10^6 \text{ coulomb/kg}$ for $\text{Hg}^{+1}$
$R$	ratio of net to total acceleration voltage, $V_I / (V_I +  V_A )$
$T$	thrust, $W(\delta/L)$ , newtons
$V_A$	deceleration voltage, v
$V_I$	net acceleration (anode) voltage, v
$\Delta V$	total acceleration voltage, $V_I +  V_A $ , v
$\Delta V_F$	filament heating voltage, v
$\Delta V_I$	discharge chamber voltage, v
$W$	thrust target weight, newtons
$\delta$	thrust target deflection, m
$\epsilon_0$	permittivity of free space, $8.85 \times 10^{-12} \text{ coulomb}^2 / (\text{newton})(\text{m})^2$
$\eta_u$	ion beam current out divided by equivalent current of neutral mercury flow in
$\tau$	period of oscillation, sec

## REFERENCES

1. Kaufman, H. R., and Reader, P. D.: Experimental Performance of an Ion Rocket Employing an Electron-Bombardment Ion Source. Paper 1374-60, Am. Rocket Soc., Inc., 1960.
2. Kaufman, Harold R.: An Ion Rocket with an Electron-Bombardment Ion Source. NASA TN D-585, 1961.
3. Reader, Paul D.: Experimental Effects of Scaling on the Performance of Ion Rockets Employing Electron-Bombardment Ion Sources. Paper 61-87-1781, Am. Rocket Soc., Inc., 1961.
4. Reader, Paul D.: Investigation of a 10-Centimeter-Diameter Electron-Bombardment Ion Rocket. NASA TN D-1163, 1962.
5. Kerslake, William R.: Accelerator Grid Tests on an Electron-Bombardment Ion Rocket. NASA TN D-1168, 1962.
6. Pawlik, Eugene V., and Wenger, Norman C.: Performance Evaluation of a Mercury-Propellant Feed System for a Flight-Model Ion Engine. NASA TN D-1213, 1962.
7. Reader, Paul D., and Finke, Robert C.: An Electron-Bombardment Ion Rocket Operating on Alternating-Current Supplies. NASA TN D-1457, 1962.
8. Kerslake, William R.: Charge-Exchange Effects on the Accelerator Impingement of an Electron-Bombardment Ion Rocket. NASA TN D-1657, 1963.
9. Keller, Thomas A.: NASA Electric Rocket Test Facilities. Seventh Nat. Symposium on Vacuum Tech. Trans., Pergamon Press, 1960, pp. 161-167.
10. Milder, Nelson L.: Comparative Measurements of Singly and Doubly Ionized Mercury Produced by Electron-Bombardment Ion Engine. NASA TN D-1219, 1962.
11. Petrov, N. N.: Secondary Emission from an Incandescent Metal Due to Action of Caesium and Potassium Ions. Fiz. tverdogo Tela, vol. 2, no. 5, May 1960, pp. 948-959. (Sci. Abs., sec. A, vol. 63, Oct. 1960, no. 15059.)
12. Pierce, J. R.: Rectilinear Electron Flow in Beams. Jour. Appl. Phys., vol. 11, no. 8, Aug. 1940, pp. 548-554.



TABLE I. - VARIATIONS OF GRID GEOMETRIES

[Standard or reference set of screen-accelerator grids has the following: hole diameters of 0.476 cm located on equilateral triangular hole spacing of 0.635 cm; screen and accelerator-grid thickness, 0.127 cm; grid open area, 40 sq cm; material, molybdenum. All dimensions are in centimeters. All grids have the same dimensions except as noted below.]

Grid set	Variation from standard	Figure number of sketch
1	Beveled screen holes, 0.112 thick screen	2(c) (33°)
2	Beveled screen holes	2(c) (45°)
3	Screen of grid set 1 reversed, 0.112 screen	2(d) (33°)
4	Screen of grid set 2 reversed	2(d) (45°)
5	Accelerator holes, 0.159 diam. with total open area of 4.4 sq cm; screen thickness, 0.147	2(b)
6	Both hole diam., 0.159; equilateral triangular hole spacing, 0.212; screen, 0.051 thick; accelerator, 0.102 thick	2(a)
7	Slotted grids, 0.476 wide slots; grid open area, 56 sq cm	2(e)
8	Thick, stainless-steel screen, 0.635 thick	2(a)
9	Graphite grids, 0.155 thick	2(a)
10	Standard grids	2(a)
11	Thrustor diam., 20; grid open area, 160 sq cm	2(a)
12	Thrustor diam., 5; grid open area, 10 sq cm	2(a)

TABLE II. - SUMMARIZED SCREEN-ACCELERATOR GRID RESULTS

Run or grid set	Center-line grid spacing, cm	Surface grid spacing, cm	Ratio of grid spacing to hole diameter		Beam current, amp	Anode potential at knee, v	Maximum anode potential breakdown (engine running), v	Ratio of net to total acceleration voltage, $R = \frac{V_I}{V_I +  V_A }$	Average bell jar pressure, torrs	Beam impingement, percent	Total run, min	Fraction of Child's law current	
			Center-line grid spacing, cm	Surface grid spacing, cm								Center-line grid spacing, cm	Surface grid spacing, cm
1	0.335	0.216	0.705	0.455	0.125	2850 2300 1550	4100 3600 >2000	0.71 .6 .4	2.6 2.9 2.2	1.3 1.6 1.4	223	0.43 .38 .38	0.18 .16 .16
2	0.498	0.371	1.050	0.780	0.125	5060 4120	>7000 >4500	0.8 .6	3.3 3.6	1.6 2.1	138	0.39 .34	0.22 .19
3(a)	0.315	0.195	0.661	0.409	0.125	1800 1500 1050	4700 3900 >2000	0.8 .6 .4	1.3 1.2 2.0	1.3 1.2 2.0	39	0.76 .65 .60	0.29 .25 .22
3(b)	0.512	0.396	1.075	0.831	0.125	3750 2850 1950	5300 4500 >2000	0.8 .6 .4	3.4 2.4 3.3	0.8 1.4 1.5	117	0.67 .65 .64	0.40 .39 .38
4(a)	0.384	0.256	0.805	0.537	0.125	2500 2000 1300	5000 4000 >2000	0.8 .6 .4	3.2 3.2 3.0	0.64 .96 1.20	70	0.68 .62 .64	0.30 .28 .29
4(b)	0.503	0.376	1.055	0.790	0.125	3800 2950	>5500 >4500	0.8 .6	4.1 3.8	1.44 1.92	60	0.63 .60	0.35 .33
5(a)	0.512	0.373	1.075	0.783	0.075	4200 3500 2700 2000	5000 4000 3000 >3500	1.0 .8 .6 .4	3.9 3.3 3.3 3.7	4.1 4.65 5.00 6.00	48	0.49 .45 .43 .37	0.26 .24 .23 .19
5(b)	0.217	0.079	0.555	0.165	0.075	4000 3020 2400 1600	4300 3500 2600 2600	1.0 .8 .6 .4	3.4 2.7 2.6 3.0	3.48 2.80 3.48 3.75	90	0.09 ↓	0.01 ↓
5(c)	0.512	0.373	1.075	0.783	0.075	-----	-----	0.62	---	44.5	45	-----	-----
6(a)	0.170	0.0865	1.07	0.545	0.080	1700	>2500	0.8	2.2	7.50	30	0.15	0.04
6(b)	0.264	0.188	1.659	1.180	0.163	1700 1400 1200	>5500 >4500 >2000	0.8 .6 .4	4.0 4.0 4.0	1.07 1.78 2.39	40	0.75 .65 .45	0.38 .35 .23
7(a)	0.447	0.323	0.937	0.677	0.125	3240 2800	>5500 >4200	0.8 .6	2.4 2.6	0.72 .96	80	0.44 .36	0.23 .19
7(b)	0.592	0.465	1.24	0.975	0.125	4300 3500	>7000 >4500	0.8 .6	4.8 4.8	1.00 1.28	75	0.57 .50	0.32 .28
8(a)	0.526	0.145	1.105	0.304	0.040	1200 950 660	4000 3000 >2000	0.8 .6 .4	5.0 5.0 5.0	1.50 1.88 2.00	80	1.22 1.14 1.07	0.09 .09 .08
8(b)	0.593	0.312	1.243	0.656	0.050	1740 1350 940	>6000 >4200 >2000	0.8 .6 .4	7.8 7.8 5.3	2.00 2.50 2.80	80	1.54 1.46 1.36	0.31 .29 .28
9(a)	0.452	0.297	0.95	0.623	0.125	3150 2450 1900	>3500 >2800 >2000	0.8 .6 .4	5.8 5.7 5.4	1.32 1.76 2.03	95	0.68 .65 .62	0.29 .27 .26
9(b)	0.520	0.368	1.09	0.772	0.125	4100 3500	>5500 >4500	0.8 .6	4.1 4.1	2.00 2.56	110	0.61 .55	0.30 .26
10(a)	0.439	0.312	0.920	0.656	0.250	4250	>6000	0.8	5.8	0.83	10	0.84	0.41
10(b)	0.360	0.234	0.755	0.491	0.125	2300 1700 1200	4500 >3000 >2000	0.8 .6 .4	4.2 3.8 3.7	1.00 1.32 1.52	125	0.68 .70 .64	0.28 .29 .27
11	0.350	0.224	0.735	0.470	0.700	3000 2500	5000 >3600	0.8 .6	<sup>a</sup> 0.57 .53	2.50 3.20	60	0.58 .49	0.24 .20
12	0.368	0.241	0.772	0.505	0.062	3600 2950	>5000 >3000	0.8 .6	5.7 6.3	1.45 .97	110	0.72 .64	0.31 .27

<sup>a</sup>Tank pressure.

TABLE III. - ORIGINAL DATA FOR SUMMARIZED RESULTS OF TABLE II

[ $\Delta V_I = -50$  v for all runs.]

Run	Anode potential, $V_I$ , v	Accelerator potential, $V_A$ , v	Beam current, $J_B$ , amp	Accelerator current, $J_A$ , amp	Anode current, $J_I$ , amp	Emission current, $J_E$ , amp	Axial magnetic field at screen, gauss	Bell jar pressure, mm Hg	Ratio of net to total acceleration voltage, $R = \frac{V_I}{V_I +  V_A }$	Discharge chamber energy, ev/ion			
1	4000	-1600	0.125	$1.78 \times 10^{-3}$	----	----	35	$2.6 \times 10^{-5}$	0.71	---			
	3000	-1200		1.45	1.4	1.1		2.4	510				
	2700	-1080		1.85	1.35	↓		2.6	490				
	2600	-1040		3.0	1.3			↓	470				
	2500	-1000		5.0	1.3	1.0			470				
	3500	-2340		2.4	1.3	↓		470					
	2400	-1600		2.05	----			3.1	---				
	2250	-1500		2.3	----	3.1		---					
	2200	-1470		4.2	----	2.3		---					
	2000	-3000		2.6	1.4	1.2		2.2	510				
	1600	-2400		1.72	1.5	1.2		2.2	550				
	1500	-2250		1.97	----	2.2		---					
	1400	-2100		4.7	----	2.2		---					
	2	7000		-1750	0.125	$2.02 \times 10^{-3}$		1.20	1.11	35	$3.0 \times 10^{-5}$	0.8	430
6000		-1500	2.05	1.29		1.18	3.3	↓	466				
5500		-1375	2.30	1.30		1.19	3.3		470				
5250		-1313	3.00	1.31		1.20	3.4		474				
5000		-1250	5.40	1.31		1.20	3.4		474				
4500		-3000	2.68	1.31		1.20	3.5	.6	474				
4300		-2860	2.83	1.35		1.22	3.7	↓	490				
4100		-2730	3.50	1.32		1.21	3.7		478				
4000		-2660	6.60	1.48		1.39	3.6	↓	542				
3(a)		4500	-1125	0.125		$0.88 \times 10^{-3}$	----		----		35	$1.2 \times 10^{-5}$	0.8
		2500	-625			.81	1.1	0.9	1.5			↓	390
		2000	-500			.77	1.2	1.0	1.4				430
	1800	-450	----		1.1	.9	1.2	390					
	1700	-425	1.07		1.2	1.1	1.3	430					
	1600	-400	3.30		1.3	1.2	----	470					
	3600	-2400	1.00		1.1	1.0	1.2	.6	390				
	1800	-1200	.73		1.2	1.1	1.1	↓	430				
	1500	-1000	.72		1.3	1.2	1.3		470				
	1400	-933	1.37		----	----	1.1	↓	---				
	1300	-867	2.56		----	----	----		---				
	2000	-3000	1.02		----	----	1.3	.4	---				
	1200	-1800	.86		1.2	----	2.0	↓	430				
	1100	-1650	.83		1.4	1.2	----		510				
	1000	-1500	1.20		1.4	1.2	----	↓	510				
	900	-1350	3.10		1.4	1.2	2.7		510				
	3(b)	5000	-1250		0.125	$1.25 \times 10^{-3}$	1.35	1.2	35	$2.4 \times 10^{-5}$		0.8	430
		3800	-950			1.05	1.30	1.2		3.6		↓	470
3700		-925	1.42	1.30		1.2	4.0	470					
3500		-875	3.63	1.20		1.1	3.6	430					
3400		-850	4.91	1.30		1.2	----	470					
4500		-3000	2.10	----		----	2.3	.6		---			
3000		-2000	1.76	1.30		1.2	2.5	↓		430			
2800		-1875	1.87	1.30		1.2	2.3			470			
2600		-1730	3.42	----		----	2.4	↓		---			
2000		-3000	1.87	1.25		1.1	3.0	.4		450			
1900		-2850	2.14	1.30		1.1	3.6	↓		470			
1800		-2700	3.63	1.25		1.1	3.0			450			
1600		-2400	12.80	1.30		1.1	3.6	↓		470			
4(a)		5000	-1250	0.125		$0.99 \times 10^{-3}$	1.12			1.02	35	$3.2 \times 10^{-5}$	0.8
		3000	-750			.82	1.49	1.38		↓		↓	537
	2500	-625	1.01		1.59	1.48	587						
	2400	-600	1.88		1.69	1.55	↓		625				
	2200	-550	5.30		1.79	1.70			666				
	4000	-2660	1.55		1.15	1.00	↓	.6	407				
	3000	-2000	1.13		1.32	1.20		470					
	2000	-1330	1.17		1.49	1.31	↓	↓	576				
	1900	-1270	1.53		1.51	1.39			550				
	1800	-1200	3.60		1.69	1.52	3.0		620				
	2000	-3000	1.73		1.22	1.02	.4	437					
	1500	-2250	1.58		1.39	1.20	↓	↓	507				
	1350	-2050	1.48		1.51	1.30			555				
	1200	-1800	3.85		1.62	1.47	↓		593				
4(b)	5500	-1375	0.125	$2.04 \times 10^{-3}$	1.00	0.92	35	$4.3 \times 10^{-5}$	0.8	350			
	3800	-950		1.85	1.25	1.19		4.0	↓	450			
	3700	-925		2.23	1.28	1.20		4.1		462			
	3500	-875		4.20	1.31	1.25		4.2		474			
	3400	-850		9.20	1.42	1.40		4.1		518			
	4500	-3000		2.70	1.02	.95		3.8	.6	352			
	3000	-2000		2.40	1.23	1.17		4.0	↓	442			
	2800	-1870		3.05	1.30	1.22		3.6		470			
	2700	-1800		4.20	1.39	1.27		---	↓	506			

TABLE III. - Continued. ORIGINAL DATA FOR SUMMARIZED RESULTS OF TABLE II

[ $\Delta V_I = -50$  v for all runs.]

Run	Anode potential, $V_I$ , v	Accelerator potential, $V_A$ , v	Beam current, $J_B$ , amp	Accelerator current, $J_A$ , amp	Anode current, $J_I$ , amp	Emission current, $J_E$ , amp	Axial magnetic field at screen, gauss	Bell jar pressure, mm Hg	Ratio of net to total acceleration voltage, $R = \frac{V_I}{V_I +  V_A }$	Discharge chamber energy, ev/ion
5(a)	5000 4000 3750 3000 3500 3000 2700 2300 2700 2400 2250 1800 2000 1600 1400 1200	0 ↓ -875 -750 -675 -575 -1800 -1600 -1500 -1200 -3000 -2400 -2100 -1800	0.075 ↓	$2.4 \times 10^{-3}$ 4.3 7.4 26.3 3.4 8.4 13.0 26.0 3.0 5.5 8.2 22.5 3.1 5.5 10.0 20.1	3.3 3.4 3.5 3.6 2.8 3.1 3.2 3.4 3.2 3.4 3.4 3.5 3.5 3.7 3.6 3.5	3.3 3.4 3.5 3.6 2.8 3.1 3.2 3.4 3.2 3.4 3.4 3.5 3.5 3.7 3.6 3.5	11.7 ↓ 10.8 11.7 ↓	$2.4 \times 10^{-5}$ 4.3 4.3 4.4 3.3 3.2 3.3 ↓ 3.8 3.6 3.8 3.6	1.0 ↓ .8 ↓ .6 ↓ .4 ↓	2150 2230 2285 2350 1820 2030 2085 2230 2085 2230 2230 2285 2285 2420 2350 2285
5(b)	1600	1000	0.075	$60.0 \times 10^{-3}$	2.3	2.2	15	---	0.62	1480
5(c)	4000 3500 3200 3000 3500 3000 2500 2000 2400 1950 1800 1700 1700 1600 1200 1100	0 ↓ -875 -750 -625 -500 -1600 -1300 -1200 -1132 -2550 -2400 -1800 -1650	0.075 ↓	$2.6 \times 10^{-3}$ 4.4 7.8 12.3 3.0 2.2 6.0 26.8 2.6 5.3 6.7 16.8 3.0 2.8 11.2 17.4	1.1 1.2 1.2 1.2 --- 2.0 2.3 1.8 1.9 1.9 1.6 1.6 1.4 1.4 1.3 1.3	1.0 ↓ --- 2.0 2.4 1.8 1.9 1.9 1.6 1.6 1.2 1.3 1.2 1.2	16.3 ↓ ↓ ↓ ↓ ↓ ↓ ↓ ↓ ↓ ↓ ↓ ↓ ↓ ↓ ↓ ↓	$3.4 \times 10^{-5}$ 3.4 3.5 3.5 2.7 ↓ 2.6 2.6 2.6 3.0 3.2 3.0 3.0	1.0 ↓ .8 ↓ .6 ↓ .4 ↓	680 750 750 750 --- 1280 1484 1150 1220 1220 1020 1020 880 880 820 820
6(a)	2000 1500 1200 800	-500 -375 -300 -200	0.080 ↓	$5.9 \times 10^{-3}$ 6.4 10.4 32.0	1.1 .95 1.3 1.5	0.9 .8 1.1 1.3	35 ↓	$2.2 \times 10^{-5}$ 2.2 2.2 2.1	0.8 ↓	637 544 763 887
6(b)	5500 3000 2000 1500 1300 4500 2000 1500 1200 2000 1500 1250 900	-1375 -750 -500 -375 -325 -3000 -1325 -1000 -800 -3000 -2250 -1975 -1350	0.163 ↓	$2.2 \times 10^{-3}$ 1.95 2.3 3.8 11.0 3.8 3.0 2.9 5.6 4.3 3.9 4.0 8.3	1.62 2.15 2.78 3.15 3.59 1.5 2.3 2.75 2.91 1.85 2.2 2.2 2.99	1.39 1.82 2.38 2.68 3.0 1.22 1.92 2.31 2.4 1.55 1.81 1.81 2.41	35 ↓ ↓ ↓ ↓ ↓ ↓ ↓ ↓ ↓ ↓ ↓ ↓ ↓	$4.0 \times 10^{-5}$ ↓ ↓ ↓ ↓ ↓ ↓ ↓ ↓ ↓ ↓ ↓ ↓ ↓	0.8 ↓ ↓ ↓ ↓ ↓ ↓ ↓ ↓ ↓ ↓ ↓ ↓ ↓	447 609 763 923 1060 413 655 794 845 503 617 625 850
7(a)	5500 3500 3300 3200 3000 4200 3000 2800 2700	-1375 -875 -825 -800 -750 -2800 -2000 -1900 -1800	0.125 ↓	$1.24 \times 10^{-3}$ .89 .98 1.83 8.1 1.6 1.21 1.37 30.0	1.2 1.3 1.35 1.35 1.4 1.55 1.3 1.35 1.35	1.2 1.3 1.35 1.4 1.55 1.3 1.35 1.4 2.0	35 ↓ ↓ ↓ ↓ ↓ ↓ ↓ ↓	$2.4 \times 10^{-5}$ ↓ ↓ ↓ ↓ 3.2 2.4 2.4 2.4	0.8 ↓ ↓ ↓ ↓ ↓ ↓ ↓ ↓	430 470 490 490 490 470 490 510 490
7(b)	7000 5000 4500 4100 3700 4500 4000 3500 3200 3000	-1750 -1250 -1125 -1025 -920 -3000 -2660 -2330 -2120 -2000	0.125 ↓	$2.15 \times 10^{-3}$ 1.31 1.33 3.5 10.0 2.0 1.73 1.78 3.5 8.2	1.11 1.35 1.35 1.41 1.59 1.3 1.39 1.50 1.52 1.59	1.11 1.38 1.39 1.43 1.59 1.34 1.40 1.50 1.55 1.6	35 ↓ ↓ ↓ ↓ ↓ ↓ ↓ ↓ ↓ ↓	$4.8 \times 10^{-5}$ ↓ ↓ ↓ ↓ ↓ ↓ ↓ ↓ ↓ ↓	0.8 ↓ ↓ ↓ ↓ ↓ ↓ ↓ ↓ ↓ ↓	390 482 490 513 577 470 502 542 548 586

TABLE III. - Concluded. ORIGINAL DATA FOR SUMMARIZED RESULTS OF TABLE II

[ $\Delta V_I = -50$  v for all runs.]

Run	Anode potential, $V_I$ , v	Accelerator potential, $V_A$ , v	Beam current, $J_B$ , amp	Accelerator current, $J_A$ , amp	Anode current, $J_I$ , amp	Emission current, $J_E$ , amp	Axial magnetic field at screen, gauss	Bell jar pressure, mm Hg	Ratio of net to total acceleration voltage, $R = \frac{V_I}{V_I +  V_A }$	Discharge chamber energy, ev/ion
8(a)	4000 2000 1500 1000 900 3000 1500 850 750 2000 1000 700 600	-1000 -500 -375 -250 -225 -2000 -1000 -570 -500 -3000 -1500 -1050 -900	0.040 ↓	$0.82 \times 10^{-3}$ .60 .59 2.3 4.1 1.35 .79 1.3 2.55 1.5 .85 .85 1.9	3.13 4.3 4.8 6.6 5.9 2.9 4.0 5.2 5.9 3.1 4.1 5.05 5.5	2.90 4.11 4.55 6.55 5.8 2.8 4.0 5.25 5.9 3.05 4.1 5.1 5.5	35 ↓	$5.0 \times 10^{-5}$ ↓	0.8 ↓ .6 ↓ .4 ↓	3800 5320 5320 8200 9320 3570 4950 6450 7320 3820 5070 6260 6825
8(b)	5000 2000 1800 1700 1600 4200 1600 1300 1100 2000 1400 1000 800	-1200 -500 -450 -425 -400 -2800 -1070 -870 -730 -3000 -2100 -1500 -1200	0.050 ↓	$1.13 \times 10^{-3}$ 1.05 1.12 1.64 2.25 1.47 1.25 1.60 6.33 1.65 1.40 1.40 3.50	4.0 6.2 6.2 6.7 6.7 3.3 6.3 6.8 8.2 4.8 5.8 6.8 7.8	3.4 6.2 6.1 6.6 6.6 3.2 6.3 6.8 8.4 4.8 5.7 6.8 8.0	35 ↓	$7.8 \times 10^{-5}$ ↓ 5.3 ↓	0.8 ↓ .6 ↓ .4 ↓	3950 6150 6150 6650 6650 3250 6250 6750 8150 4750 5750 6750 7750
9(a)	3500 3200 3000 2800 2800 2500 2400 2000 2000 1700 1500	-875 -800 -750 -700 -1870 -1670 -1600 -1330 -3000 -2550 -2250	0.125 ↓	$1.65 \times 10^{-3}$ 1.93 3.6 10.2 2.24 2.2 2.71 26.5 2.63 2.8 10.0	1.93 2.1 2.15 2.41 1.93 2.05 2.05 2.90 1.93 2.1 2.39	1.54 1.71 1.71 2.0 1.52 1.65 1.65 2.39 1.54 1.69 1.92	35 ↓	$5.8 \times 10^{-5}$ 5.7 5.8 5.8 5.7 ↓ 5.4 5.4 5.4	0.8 ↓ .6 ↓ .4 ↓ .4 ↓	721 790 810 913 721 730 730 1110 721 790 906
9(b)	4500 4000 3700 3500 3500 2900 2700 2500	-1125 -1000 -925 -875 -2330 -1940 -1800 -1660	0.125 ↓	$2.5 \times 10^{-3}$ 3.2 5.7 9.7 3.2 2.02 2.15 2.62	1.71 1.9 1.95 2.1 1.79 1.69 1.79 2.21	1.34 1.53 1.6 1.71 1.4 5.3 8.6 25.3	35 ↓	$4.1 \times 10^{-5}$ ↓ 3.9 4.1 4.1	0.8 ↓ .6 ↓	635 710 730 790 667 627 667 834
10(a)	6000 5000 4500 4300 4000	-1500 -1250 -1125 -1075 -1000	0.250 ↓	$2.1 \times 10^{-3}$ 2.0 2.1 2.1 5.2	4.1 4.65 4.95 4.7 5.15	3.25 3.7 4.0 3.8 4.2	35 ↓	$5.8 \times 10^{-5}$ ↓	0.8 ↓	770 880 940 890 980
10(b)	4500 2400 2200 2000 3000 2000 1700 1600 2000 1400 1200 1100	-1125 -600 -550 -500 -2000 -1335 -1135 -1070 -3000 -1950 -1800 -1650	0.125 ↓	$1.37 \times 10^{-3}$ 1.27 1.90 7.40 1.70 1.64 1.77 3.85 2.00 1.94 2.08 4.10	1.68 2.28 2.35 2.53 1.80 2.30 2.32 2.45 1.87 2.17 2.30 2.45	1.38 1.97 1.90 2.27 1.50 1.80 1.95 2.15 1.53 1.80 1.95 2.08	35 ↓	$4.4 \times 10^{-5}$ 4.0 4.0 4.3 4.0 3.8 3.6 3.6 3.7 3.6 3.7	0.8 ↓ .6 ↓ .4 ↓	623 863 890 962 670 870 878 929 698 819 870 930
11	5000 4200 3000 2500 3600 3000 2700 2400	-1250 -1050 -750 -625 -2400 -2000 -1800 -1600	0.700 ↓	$17.30 \times 10^{-3}$ 25.00 49.00 61.00 23.20 26.50 31.00 43.00	10.90 12.00 12.50 12.30 10.90 11.30 11.50 12.10	8.30 9.50 9.80 9.70 8.30 8.80 8.90 9.50	10 ↓	$0.71 \times 10^{-5}$ ↓ .60 .52 .45 .62 .53 .51 .47	0.8 ↓ .6 ↓	728 807 843 828 728 758 773 815
12	5000 4000 3750 3600 3500 3000 3900 3500 3000 2850 2700	-1250 -1000 -940 -900 -875 -750 -2600 -2200 -2000 -1900 -1800	0.062 ↓	$0.43 \times 10^{-3}$ 1.08 1.4 2.4 2.9 16.0 1.05 .95 1.12 1.5 4.6	0.85 .9 .99 1.05 1.03 1.32 .9 .95 1.0 1.0 1.19	0.88 1.88 1.05 1.15 1.15 1.48 .99 1.01 1.08 1.1 1.35	105 ↓	$2.6 \times 10^{-5}$ 2.8 7.0 6.8 7.0 7.8 6.6 6.4 5.9 6.2 6.4	0.8 ↓ .6 ↓	686 726 798 846 830 1065 726 766 806 806 959

<sup>a</sup>Tank pressure.

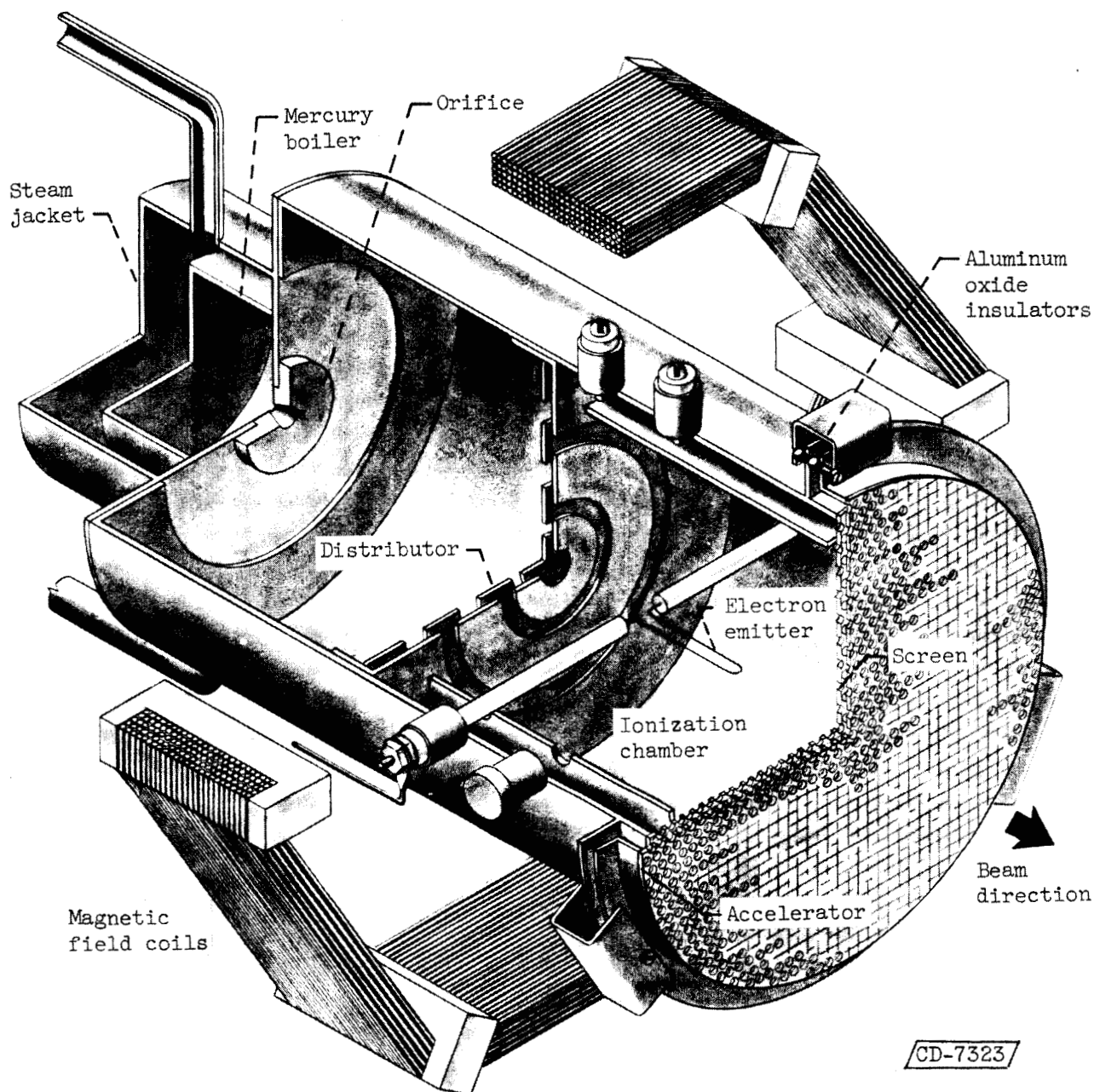


Figure 1. - Cutaway sketch of 10-centimeter-diameter electron-bombardment thruster.

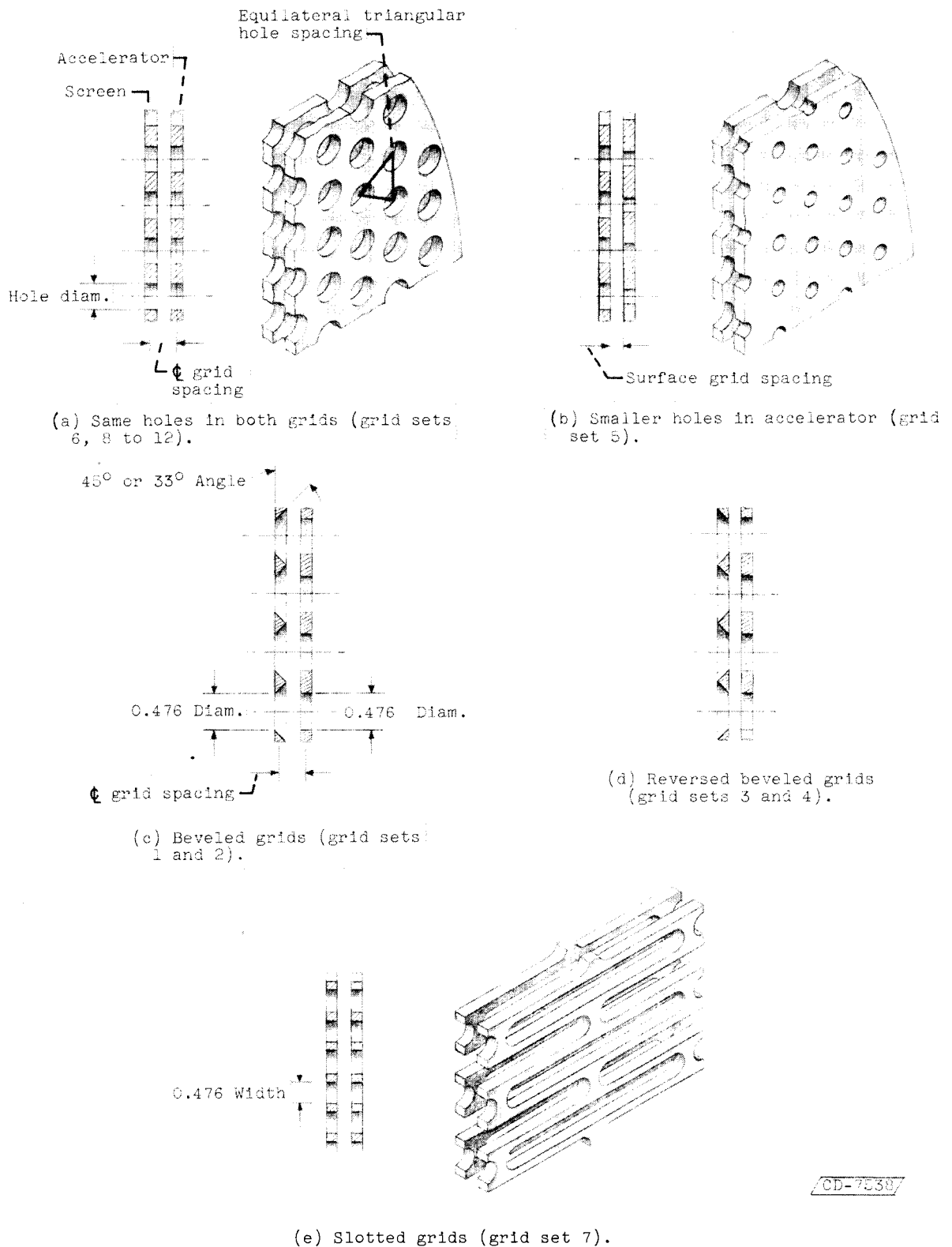


Figure 2. - Details of screen and accelerator grids. (All dimensions in cm.)

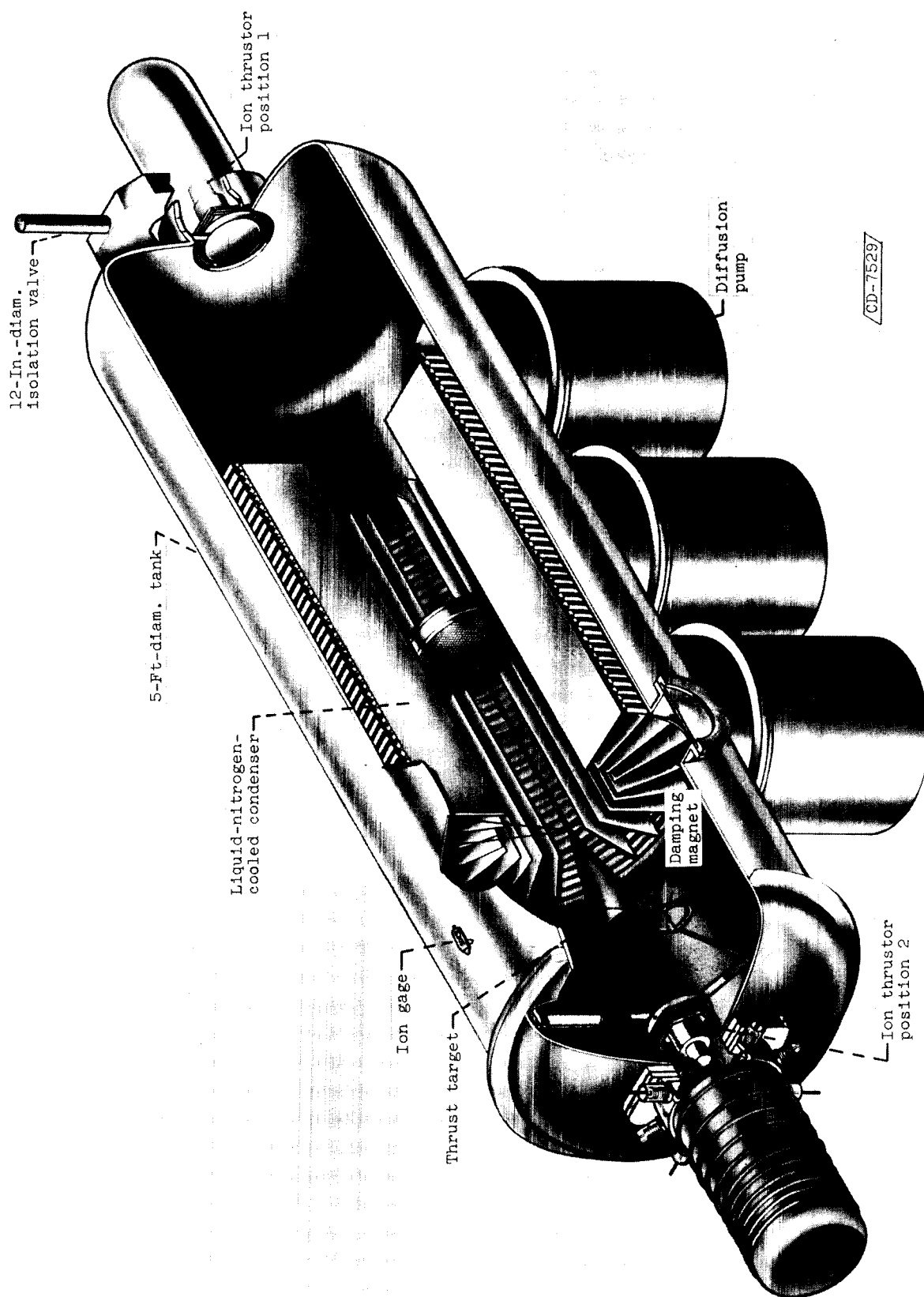


Figure 3. - Thruster and thrust target positions in vacuum tank.



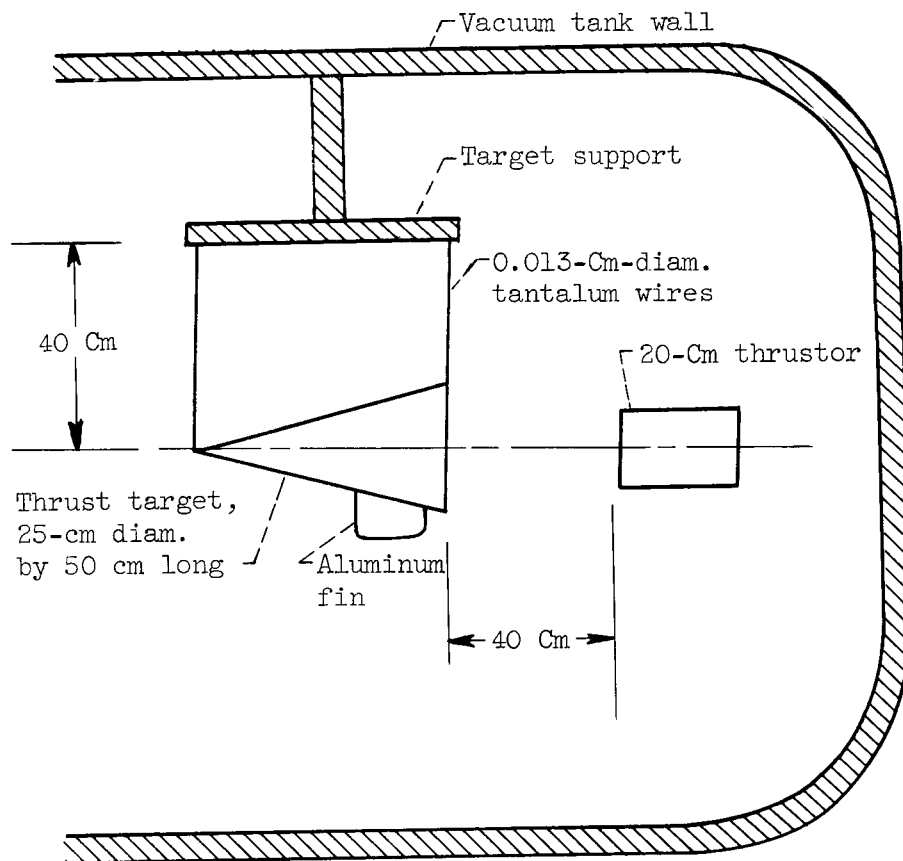


Figure 4. - Thrust target installation in vacuum tank.

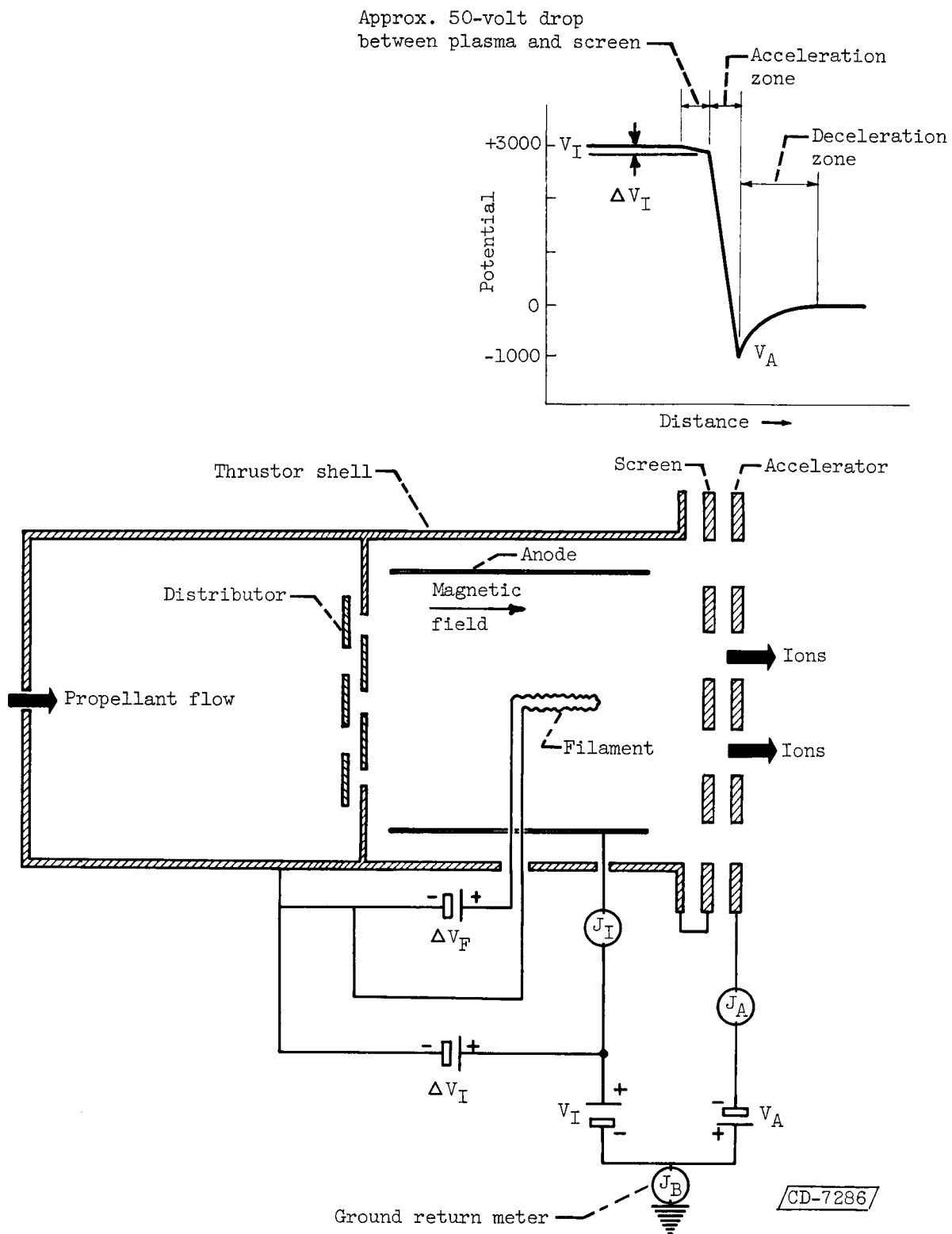
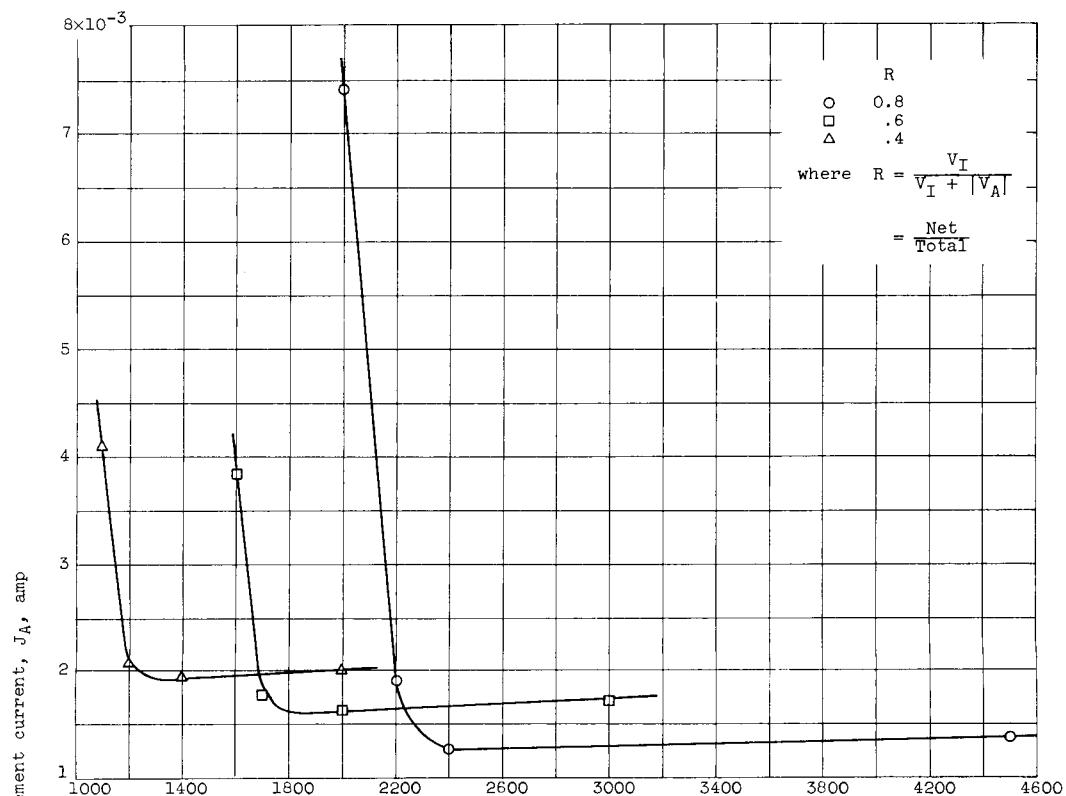
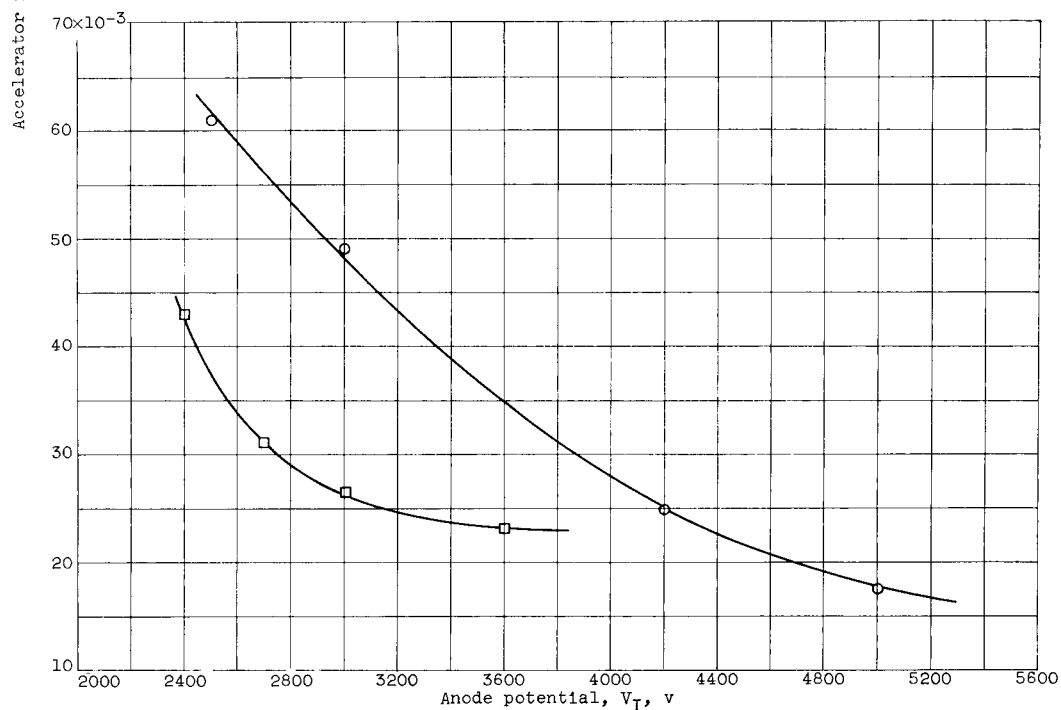


Figure 5. - Schematic electrical diagram and potential profile of ion thruster with an electron-bombardment ion source.



(a) 10-Centimeter-diameter ion source using number 10 grids. Ion beam current, 0.125 ampere.



(b) 20-Centimeter-diameter ion source using number 11 grids. Ion beam current, 0.700 ampere.

Figure 6. - Typical data of accelerator impingement currents plotted against anode potential.

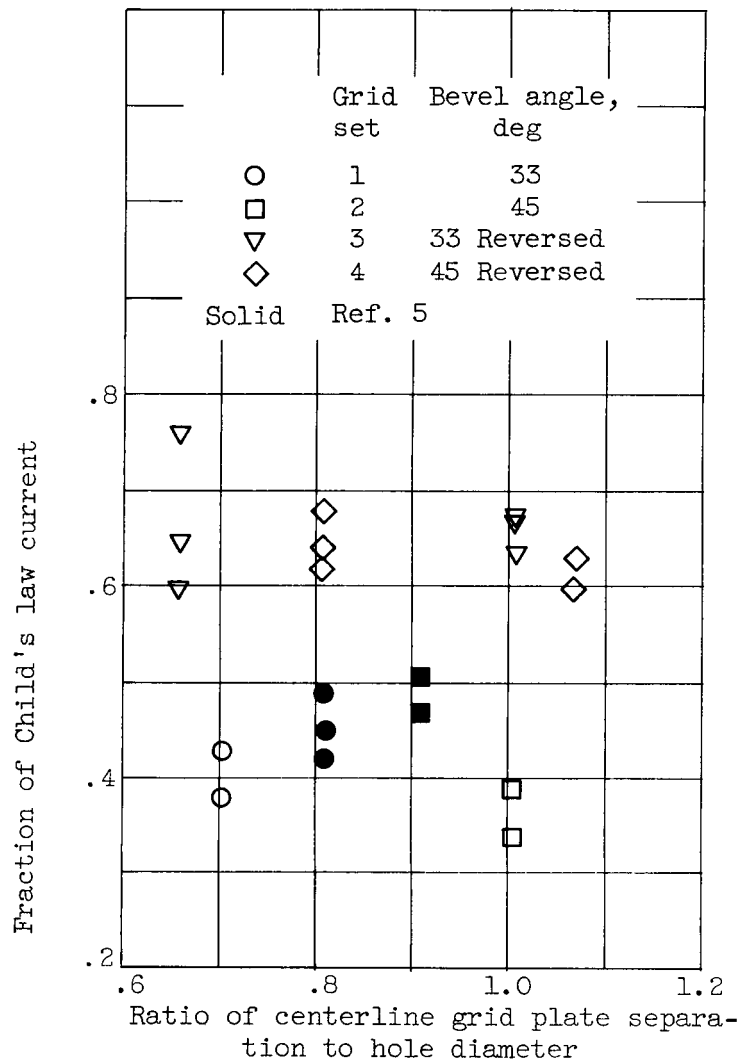
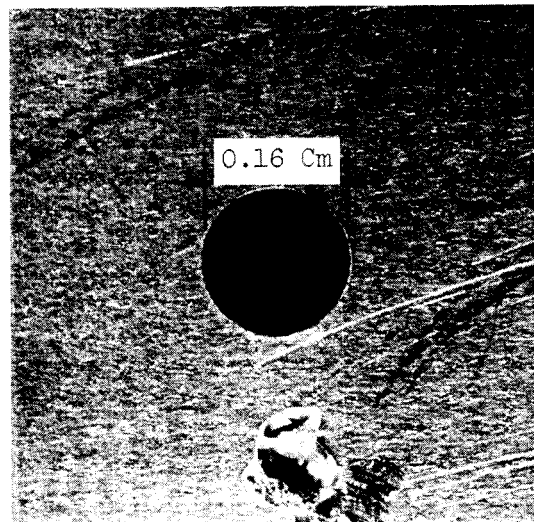
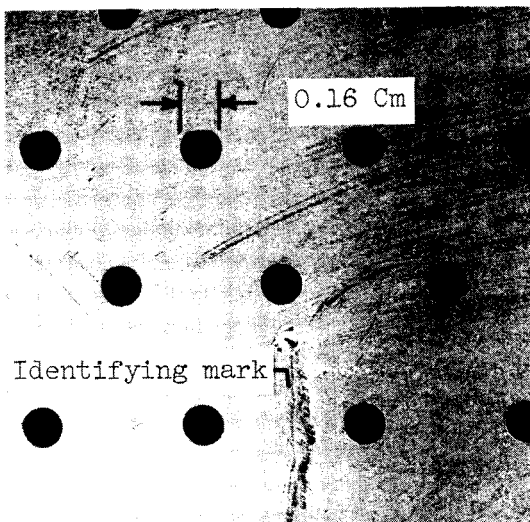
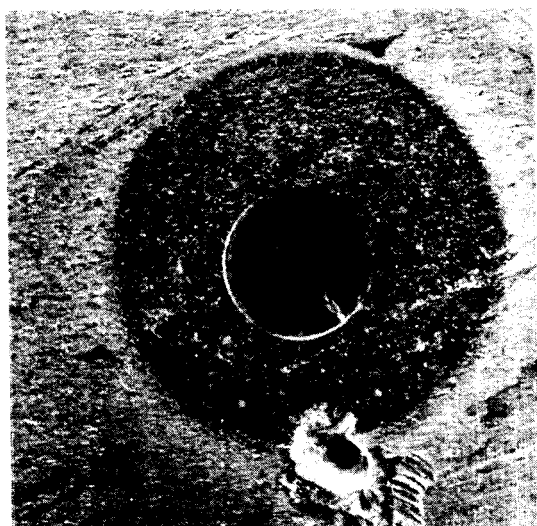


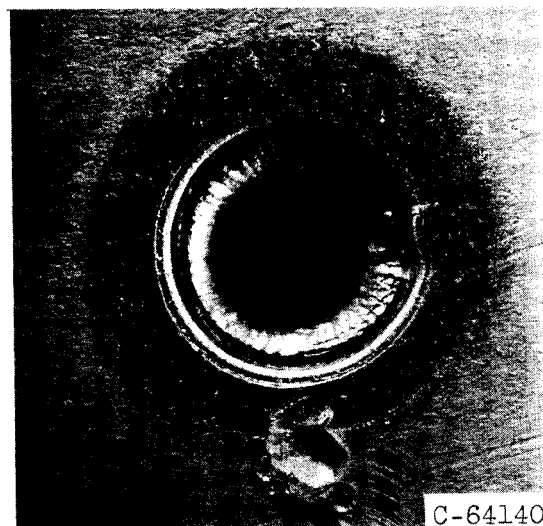
Figure 7. - Fraction of Child's law current passing through beveled screen-accelerator grids of 10-centimeter-diameter thruster.



(a) Before testing.



(b) After run 5(b).



(c) After run 5(c) of 45 minutes of high impingement.

Figure 8. - Upstream face of molybdenum accelerator grid used in run 5.

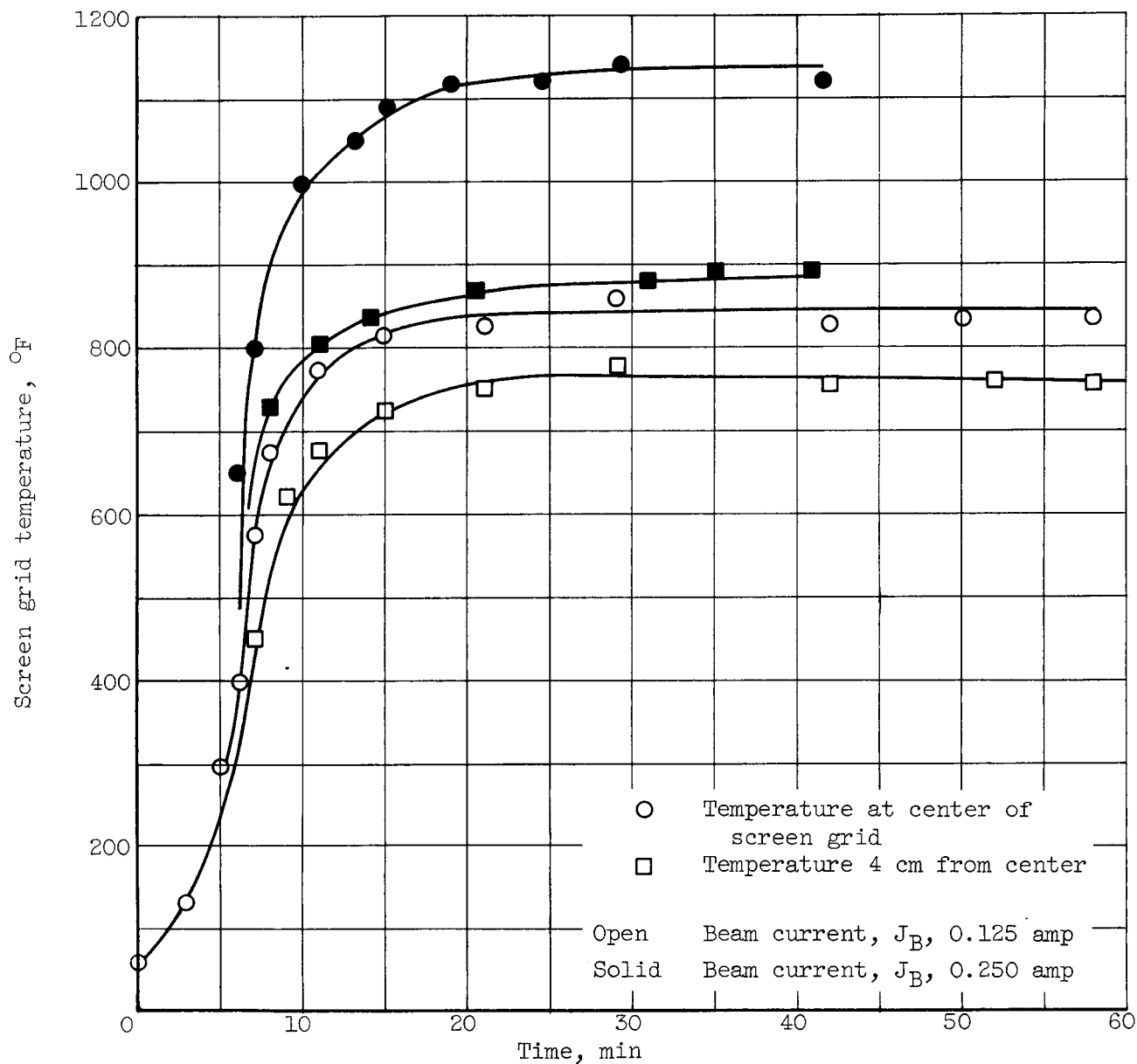


Figure 9. - Heating curves for two thermocouple locations on screen grid for beam currents of 0.125 and 0.250 ampere.

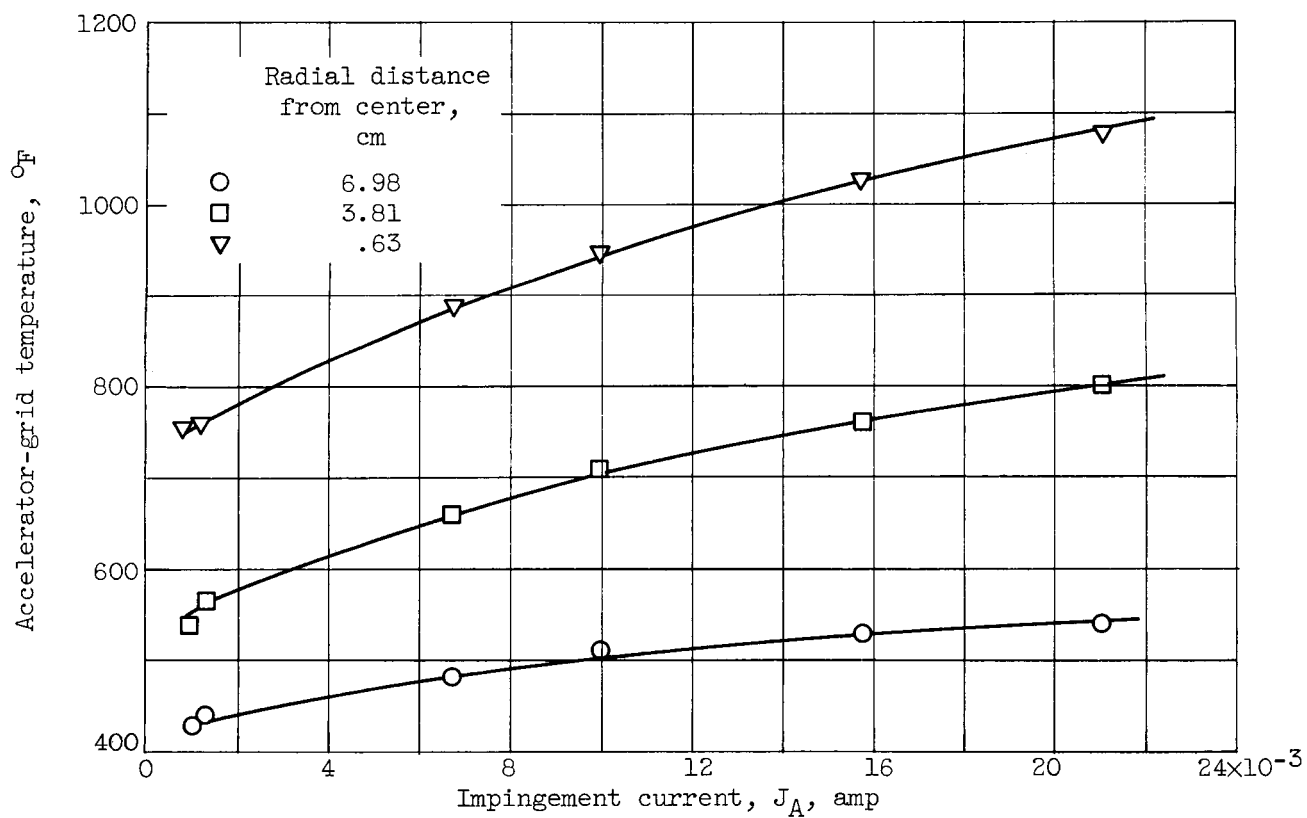


Figure 10. - Steady-state accelerator-grid temperature plotted as a function of accelerator impingement current.

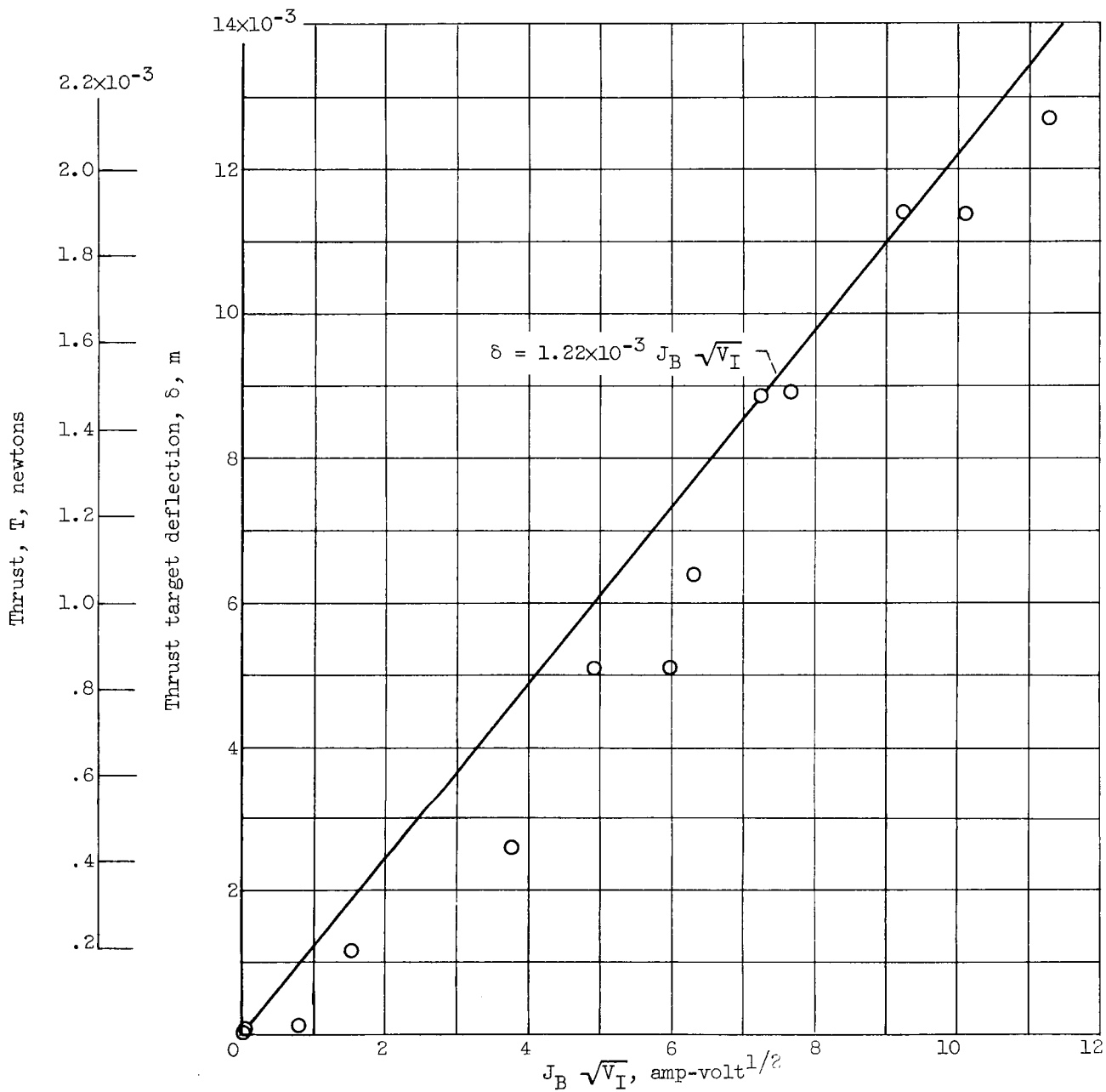


Figure 11. - Thrust target deflection as a function of thruster output parameter.